Fault-Tolerant Architectures With Enhanced Bus Protection for Electric/Hybrid Aircraft Systems

Anil Kumar Reddy Siddavatam⬢, *Graduate Student Member, IEEE*, Kaushik Rajashekara⬢, *Life Fellow, IEEE*, Ravi Prakash Reddy⬢, Hao Huang⬢, *Life Fellow, IEEE*, Harish S. Krishnamoorthy, *Senior Member, IEEE*, Zhou Dong⬢, *Member, IEEE*, and Fei Wang⬢, *Fellow, IEEE*

Abstract— This article introduces two electrical architectures for electric/hybrid-electric aircraft propulsion systems to address the issues of the radial baseline architecture, where a single bus feeds the four propulsion motors. A fault on this bus results in complete isolation of the bus, to which propulsion motors are connected. By using the proposed architectures, the fault can be isolated without having to disconnect all the propulsion motors. This would increase the reliability, redundancy, and robustness of the electrical system and/or avoid oversizing the components present in the architecture. In this article, the protection strategy and action of circuit breakers are discussed for different fault conditions. The enhanced fault-tolerant operation of the proposed architectures over the existing radial baseline architecture for the electrified aircraft propulsion (EAP) system is validated for both open-circuit and short-circuit faults at different locations in the system, using controller hardware in the loop (HIL) results obtained using typhoon HIL testbed. Furthermore, the feasibility analysis of interconnecting the individual propulsion channels to reduce the oversizing of components is also discussed.

Index Terms— Circuit breakers, electric aircraft, electric motors, power electronic converters.

I. Introduction

CO_2 EMISSIONS from aircraft systems account for about 3% of total global CO_2 emissions and about 9% of the CO_2 emissions from all transportation sources. Large commercial aircraft systems (single-aisle and twin-aisle with a capacity of more than 100 passengers) contribute to most of the CO_2 emissions in global commercial aviation; hence, it will be most useful to concentrate research efforts on clean technologies applicable to these large aircraft systems [1], [2]. According to figures published by the European Environment Agency, air travel emits the highest level of CO_2 with 285 g/passenger km, while rail travel emits 14 g/km and road travel emits 158 g/km. Hence, to reduce the emissions, the trend is shifting from

more electric aircraft (MEA) systems to electric and hybrid propulsion-based systems [3]. Several companies and organizations like NASA are developing electric and hybrid propulsion systems to replace the turbine-driven propulsors and enable the advantages of boundary layer ingestion (BLI) and distributed propulsion, which considerably reduce both fuel burns and CO_2 [4]. To meet the power requirements for propulsion, the rating of the electric motors for driving the propulsor has to be of the order of megawatts (MW). Hence, to minimize the current and thus reduce the size of the cables, the system voltage has to be high (a few kilovolts), depending on the size of the motors and the aircraft. Consequently, operating at higher voltage enables better performances in terms of lower weight, higher efficiency [5], and so on.

Various architectures are investigated in the literature to identify the most promising technologies for the all electric aircraft/hybrid electric aircraft (AEA/HEA) propulsion systems to reduce system weight [6], [7]. Barzkar and Ghassemi [8] present an overview of architectures for electric power systems in more electric and AEA and discuss on the challenges to be addressed for the proper operation of AEA over the commercial aircraft. The review of components that include power electronic converters, motors, generators, circuit breakers, and cables is also discussed in this article. The comparison between different architectures in terms of various figures of merit, such as efficiency, power density, and reliability, for AEA systems is presented in [9]. A control scheme for fault tolerant operation of advanced power generation center in case of ac–dc converter failure for MEA is reported in [10]. Discussion on possible architectures for all electric, turboelectric, and hybrid aircraft that can be made feasible in the next 20 years is also outlined in [11]. Flynn *et al.* [12] present a fault management design for electric aircraft propulsion systems that prevent the faults in the system from causing loss of critical flight functionalities and aircraft propulsion. Venuturumilli *et al.* [13] present a fault management system to address short-circuit faults in turboelectric aircraft propulsion systems, where superconducting fault current limiters are integrated into the system, thereby reducing the rating of switchgear required. Methodology to address the challenges involved in the design of fail-safe electric architectures for electrical power systems in aircraft is also presented in [14].

The electric aircraft architectures can be implemented as all-electric, parallel hybrid, series hybrid, series/parallel hybrid, turboelectric, and partial turboelectric systems. Boeing Subsonic Ultra Green Aircraft Research (SUGAR) volt, UTRC, and Rolls-Royce EVE use parallel hybrid architecture, Boeing SUGAR freeze and NASA STARC-ABL use partial turboelectric, and NASA N3-X, ESAero uses fully turboelectric architectures [15], [16], [17], [18]. NASA X3 employs a turboelectric distributed propulsion architecture that uses HVDC radial architecture, consisting of 14 propulsion motors with four buses (three motors per bus for two buses and four motors per bus for two buses) [19], [20]. To address the asymmetrical thrust issues (considering bus and generator faults) in this architecture, the number of motors is increased to 16 [21], which results in four motors for each bus. This kind of bus faces an unprecedented situation that the conventional aircraft systems and MEA systems never have had before: there are four motors, each of 1 MW rating is connected to it, and hence, the size and spreading area of the bus is much larger than that of any conventional aircraft. Thus, this radial architecture is much more vulnerable to faults for the electrified aircraft propulsion (EAP) application, and if a fault occurs in this bus, it can lead to complete isolation of the bus and disconnect all the four propulsion motors from the system. Accordingly, various components in the architecture that include motors, generators, circuit breakers, and power converters need to be oversized to meet the power demand in case of faults in the system [21]. Various architectures are introduced to overcome the issues associated with the radial architecture, such as inner bus tie, bus multifeeder, cross redundant multifeeder, and bus inner tie multifeeder architectures [20], [21], [22]. In [20], an inner bus tie architecture is presented, in which two main buses are interconnected to reduce the oversizing of the propulsion motors. However, this also suffers from the drawback of isolation of all the four propulsion motors in the event of a bus fault. In [21] and [23], a four-bus inner bus tie multifeeder turboelectric distribution propulsion architecture is presented, where each propulsion motor is provided with two redundant cables for increased reliability against the bus faults. However, this doubles the length of cables and the number of circuit breakers on the distribution network, resulting in the increase of the overall system weight. To mitigate the abovementioned issues, this article proposes two electric aircraft architectures using the loop-type structure. The concept of a ring bus (loop type) system is available in different applications like micro grids. In [24], the ring is formed between photovoltaic (PV) plant, grid, and the loads, where each load is supplied by two feeders. In [25] and [26], each load in the system has been provided by two feeders and each feeder is supplied by different sources (solar, wind, ac grid, etc.). However, this system leaves the load idle if two of these feeders are out of service. In the proposed architectures, using loop-type structure and creating the loop for the entire system (loop in loop—consists of four individual channels), each distribution network is connected with four feeders. Both the architectures can protect the system from main bus faults without disconnecting the propulsion motors, and due to the loop in loop structure, the oversizing of components (motors, circuit breakers, cables, and dc/ac converters) can be significantly reduced. This helps in reducing the weight as well as improved performance and efficiency. Thus, the salient features of the proposed work include the following.

1) This article proposes two architectures, namely, proposed fault tolerant architecture 1 (PFTA 1) and proposed fault tolerant architecture 2 (PFTA 2), in order to overcome the limitations, present in the radial baseline architecture for electric aircraft. By using the loop-type structure in PFTA 1, faults in the system can be addressed by operating appropriate circuit breakers and thus isolating the faulty section, without disconnecting propulsion motors.

2) Due to the absence of T-junction in PFTA 2, the possibility of fault at certain locations that require operation from generator of another independent channel is avoided. The number of circuit breakers required is also reduced by a quantity of four in PFTA 2, when compared to that of PFTA 1. Both the proposed architectures aid in reducing the oversizing of various components present in the system.

3) Comparative analysis regarding the required oversizing and weight of various components present in all the three architectures and the overall weight savings for the proposed architectures are also highlighted in this article.

This article is divided into the following sections. In Section II, the radial baseline architecture is discussed, and then, the proposed architectures 1 and 2 are described in Section III addressing the issues with radial baseline architecture. Section IV describes the protection coordination strategy for the proposed architectures, and in Section V, the oversizing of components for all three architectures is discussed. The validation of the proposed architectures using controller hardware in the loop (CHIL) with typhoon HIL testbed is performed in Section VI. Finally, this article is concluded in Section VII.

II. RADIAL BASELINE ARCHITECTURE FOR EAP SYSTEMS

Fig. 1 shows the typical radial baseline architecture existing in the literature for EAP systems [16]. It consists of four independent distributed propulsion channels. Each propulsion channel consists of a generator, battery bank, power converters (front end active rectifier, dc–dc converter, and dc–ac converters), nonpropulsion (NP) loads, transmission network, distribution networks, circuit breakers [CBX in Fig. 1 represents both positive (CBX_P) and negative (CBX_N) cable circuit breakers, where $x = 1, 2, 3, \ldots$], and four propulsion motors. The output of the front-end active rectifier is connected to the main bus through the transmission network. Each propulsion motor is fed from a dc–ac converter, whose input is connected to the main bus through a distribution network. The dc–dc converter interfaced to the battery bank is used to increase the battery voltage to a desired output dc voltage and is also used to regulate the main bus voltage. The generators G1 and G2 along with their respective ac–dc converters are located in the left wing and generators G3 and G4 with their respective ac–dc converters are located in the right wing. The motors
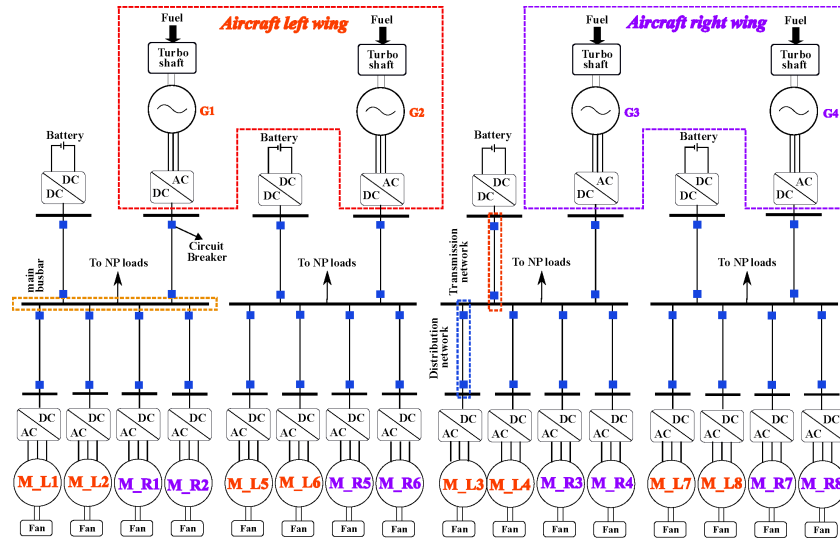
Fig. 1.   Radial baseline electrified aircraft architecture.

M_Lx and M_Rx ($x = 1, 2, \ldots, 8$) are placed in the left and right wings along with the dc–ac converters, and the rest of the components are placed in the fuselage of the electric aircraft. In each propulsion channel, two motors are placed on the left wing, while the other two are placed on the right wing to maintain the balance during an outage of one generator. The battery energy storage system (BESS), which is connected to the main bus, as shown in Fig. 1, is designed to run the aircraft in an emergency for a safe landing and also provides peak power to supplement the generator power in case required.

The main bus requires the complete isolation of the bus and the disconnection of all four healthy propulsion motors if there is a fault in the main bus of radial baseline architecture shown in Fig. 1, and this could be due to positive to negative, or positive to ground, or negative to ground faults. This results in an increased burden on the remaining 12 motors to provide the thrust required by an aircraft as four of the motors are disconnected and also requires the oversizing of generators from the remaining three channels to deliver the required power. This issue about the oversizing of the generators is addressed in [15]. As a result, the oversizing of the motors, converters, circuit breakers, and cables is also required in this case, since each motor has to deliver more power than in the case of healthy condition.

Considering the outage of one generator, which leads to the isolation of the one whole propulsion channel, the aircraft must be powered using the generators of the remaining three healthy channels. In this case, the disconnection of all the four healthy motors should still happen (in the channel where generator outage occurs) and the power to the aircraft should be supplied by the generators from the remaining three channels. This again results in the oversizing of all the components present in the system to maintain the same reliability, redundancy, and robustness. Similarly, if the outage of two generators is considered, this leads to the isolation of two individual propulsion channels, thereby resulting in even more oversizing of all the components. Thus, it can be seen that fault-tolerant operation of the existing architectures requires oversizing of

all the components in the aircraft, resulting in increased weight and cost of the whole system. To address these drawbacks, two modified architectures are proposed in this article, the details of which are given in Section III.

III. PROPOSED ELECTRIFIED AIRCRAFT ARCHITECTURES

Figs. 2 and 3 show the schematics of the proposed electric aircraft system architectures 1 and 2 (PFTA 1 and PFTA 2), respectively. Only one independent distributed propulsion channel out of four channels is shown in these figures. By using the loop-type structure in the proposed architecture, the fault at any point in the loop can be taken care of by operating the appropriate circuit breakers near the fault and thus isolating the fault area. Consequently, all the motors or most of the motors will be able to operate continuously as normal, and the reliability, redundancy, and robustness will be maximized. With the proposed architectures 1 and 2, the motors isolated under fault conditions can be operated using generators from other propulsion channels by interconnecting the individual channels through the tiebreaker. This gives more flexibility in terms of using the healthy motors of the affected channel when compared with the existing radial baseline architecture. In Figs. 2 and 3, the tiebreakers are used to connect two adjacent propulsion channels. The enhanced fault-tolerant operation of the proposed architectures over the radial baseline architecture can be well understood, by considering faults at different locations, as discussed in the following sections.

A. Fault on the Main Bus

For a short-circuit or open-circuit fault in the bus between any of the two rails (positive/negative/ground), it may be noted that the circuit breakers in both the positive and negative rails CBX_P and CBX_N (where $X = 1, 2, 3, \ldots$) need to operate. If only one of the circuit breakers (CBX_P or CBX_N) is operated, then the ground wire of the cable carries fault current, and the ground wires are generally not designed to carry such
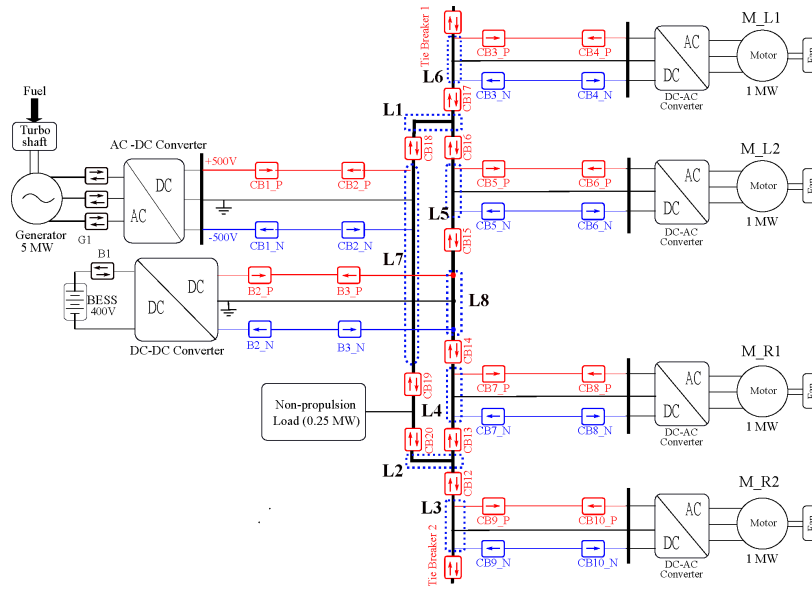
Fig. 2. Proposed fault tolerant electrified aircraft architecture 1 (PFTA 1).
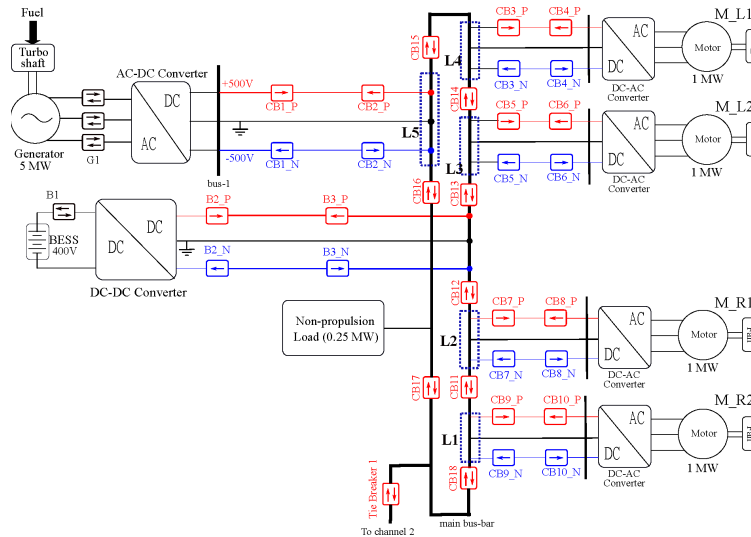

Fig. 3. Proposed fault tolerant electrified aircraft architecture 2 (PFTA 2).

high currents. Consider a bus fault in architecture 1 at location L1, as shown in Fig. 2. This results in the increase of fault current in the system, and to prevent this from damaging the cables, circuit breakers CB16, CB17, and CB18 are tripped. However, with the proposed architecture, the motors M_L2, M_R1, and M_R2 can still operate since the loop provides an alternate path for motors to receive power. It may be noted that motor M_L1, which is isolated from the channel, can also be operated by the generator of the other independent channel using tiebreaker 1. Similarly, for fault at location L2, as shown in Fig. 2, all the four motors can still be in operation using tiebreaker 2. If the fault occurs at any of the locations L3, L4, L5, or L6, architecture 1 loses only one of the motors. For this case, the functioning of architecture 1 is explained by considering a fault at location L5. Due to this fault, the circuit breakers (CB15 and CB16) adjacent to the fault location are

tripped, and to protect the cable from short-circuit currents from the input dc link capacitor of the dc–ac converter, the circuit breakers CB6_P and CB6_N are tripped. If a fault occurs at location L7, then the circuit breakers CB1_P, CB1_N, CB18, and CB19 should trip, which leads to the isolation of the generator. The circuit breakers CB1_P and CB1_N are tripped to limit the short-circuit currents from the output of the front-end active rectifier. This case (isolation of generator) is explained in Section III-B.

In the event of an open-circuit or short-circuit fault occurring concurrently at locations L5 and L6, the circuit breakers CB15, CB16, CB17, CB4_P, CB4_N, CB6_P, and CB6_N will be tripped to isolate the fault section as well as the motors M_L1 and M_L2; however, the motors M_R1 and M_R2 can still be in operation as the fault is isolated. Considering another simultaneous fault at locations L6 and L7 and then the circuit

breakers CB1_P, CB1_N, CB17, CB18, and CB19 will be tripped, which will isolate the generator of the channel and by using the tiebreaker 2, the generator of other channel is connected to restore the power to the healthy motors. In PFTA 2 shown in Fig. 3, the control strategy for a fault occurrence at locations L1, L2, L3, or L4 is the same as that discussed for the fault at locations L3, L4, L5, or L6 of PFTA 1, and for simultaneous faults at locations L3 and L4 of PFTA 2, the operation of the system is similar to that of the PFTA 1, which isolates the motors M_L1 and M_L2 and providing power to the healthy motors M_R1 and M_R2. From the above fault cases, it is clear that each channel can still be operated using three or all the four motors, using the PFTA 1 and 2, whereas none of the motors of the individual channel can be operated with the radial baseline architecture.

B. Generator Outage

If power flow from the generator to the main bus is interrupted because of the fault as mentioned in Section III-A (fault at location L7 in architecture 1) or due to any fault that requires isolation of the generator, then it is considered as generator outage. In this situation, the generator cannot provide power to the propulsion motors. In both architectures 1 and 2, if one of the generators is considered out of service, then the power should be supplied to the healthy propulsion motors of the affected channel using the generators from other channels. This can be done by interconnecting the individual channels. In the case of both bus faults and generator outage, this interconnection helps in providing power to the healthy motors from the other channels and also helps in reduction of oversizing the motors, dc–ac converter, circuit breakers, and cables; the details of which are explained in Section IV. If only two generators out of four are considered operating, then all the eight motors of the two unhealthy channels are powered using these two generators, which increases the burden on generators. Considering this burden, each generator in both architectures 1 and 2 is oversized twice to meet the load requirements (propulsion motors), which are also the same in the case of radial baseline architecture. These two oversized generators provide power to their respective propulsion motors as well as the healthy propulsion motors of the affected channels.

Hence, for the bus faults and generator outage, the proposed architecture 1 is capable of providing continuous power supply to the healthy propulsion motors (except for the propulsion motors connected to fault locations), but in one particular case of architecture 1, the fault at either of the locations L1 or L2 and motors M_L1 or M_R2 needs to be operated using the generator of another channel as the circuit breakers (CB16, CB17, and CB18 for fault at location L1 or CB12, CB13, and CB20 for fault at location L2) are tripped to isolate this fault. To overcome this, architecture 2 is proposed and is shown in Fig. 3, where the location L1 is eliminated by creating a complete loop at the main bus, and hence, this fault case is not applicable in the case of architecture 2. The operation of architecture 2 is similar to that of the operation of architecture 1. The circuit breakers CB14 and CB15 of architecture 2 can be

TABLE I
ACTION OF FAULT AT DIFFERENT LOCATIONS

Location	Baseline	PFTA -1	PFTA -2
L1	A fault at any of the location LN (N= 1,2….8) is considered as main bus fault. Circuit breakers CB1, CB3, CB4, CB7, CB9 and B2 are tripped	CB16, CB17, CB18	CB11, CB18
L2		CB12, CB13, CB20	CB11, CB12
L3		CB12	CB13, CB14
L4		CB13, CB14	CB14, CB15
L5		CB15, CB16	CB15, CB16
L6		CB17	-
L7		CB18, CB19	-
L8		CB14, CB15	-

used as backup protection if circuit breakers CB3_P or CB3_N fail to operate for faults on the distribution network connecting motor M_L1. Similarly, for distribution networks connecting motors M_L2, M_R1, and M_R2, the corresponding circuit breakers on the main bus (CB13 and CB14 for distribution network 2, CB11 and CB12 for distribution network 3, and CB11 and CB18 for distribution network 4) can be used as backup protection. For architecture 1, the backup protection is similar to that of architecture 2, whereas in the case of radial baseline architecture, the bus needs to be isolated if any of the circuit breakers fails to operate, and hence, all healthy motors will be disconnected. Table I shows the circuit breaker action for faults at different locations for all the three architectures.

The relative advantages and disadvantages of both the architectures are also summarized in the following.

1) Architecture 1 (PFTA 1): Advantage: In case of isolation of both the motors M_L1 and M_R2, the generator of that particular propulsion channel will still be able to power the remaining healthy motors, thereby removing extra burden on the battery.

Disadvantage: If fault occurs either at location L1 or L2, motors M_L1 and M_R2 need to be operated using the generator of another channel as the circuit breakers (CB16, CB17, and CB18 for fault at location L1 or CB12, CB13, and CB20 for fault at location L2) are tripped to isolate this fault. PFTA 1 requires one additional circuit breaker for each independent propulsion channel, thus requiring a total of four additional circuit breakers, when compared to that of PFTA 2.

2) Architecture 2 (PFTA 2): Advantage: Due to the absence of T-junction, the possibility of the faults at locations L1 and L2 present in PFTA 1 is avoided.

Disadvantage: In case of isolation of both of the motors M_L1 and M_R2, battery alone needs to power the healthy motors M_L2 and M_R1.

IV. PROTECTION COORDINATION CONTROL STRATEGY

The action of circuit breakers for faults at different locations in architectures 1 and 2 is shown in Table II. Based on the direction of the fault currents, unidirectional and bidirectional circuit breakers are used. Unidirectional circuit breakers are represented with a single arrow and bidirectional circuit breakers with two anti-parallel arrows, as shown in

TABLE II
ACTION OF CIRCUIT BREAKERS

S.no	Fault type	PFTA -1	PFTA -2
1	Generator Output terminals shorted	AC circuit breaker G1	AC circuit breaker G1
2	Front end active rectifier input A phase terminal shorted	A-phase CB of G1 - open	A-phase CB of G1 - open
3	Front end active rectifier input terminals shorted (2-phases)	all phase CB's of G1 - open	all phase CB's of G1 - open
4	Cable located between CB3 and CB4 is shorted	CB3, CB4	CB3, CB4
5	Cable located between CB5 and CB6 is shorted	CB5, CB6	CB5, CB6
6	Cable located between CB7 and CB8 is shorted	CB7, CB8	CB7, CB8
7	Cable located between CB9 and CB10 is shorted	CB9, CB10	CB9, CB10
8	DC/AC converter input terminals shorted in distribution network 1	CB3 and DC/AC converter	CB3 and DC/AC converter
9	DC/AC converter input terminals shorted in distribution network 2	CB5 and DC/AC converter	CB5, and DC/AC converter
10	DC/AC converter input terminals shorted in distribution network 3	CB7 and DC/AC converter	CB7 and DC/AC converter
11	DC/AC converter input terminals shorted in distribution network 4	CB9 and DC/AC converter	CB9 and DC/AC converter
12	Motor input terminals shorted	DC/AC converter	DC/AC converter
13	DC/DC converter input terminals shorted	DC/DC converter, B1	DC/DC converter and B1
14	DC/DC converter output terminals shorted	DC/DC converter, B2	DC/DC converter, B2
15	Short circuit between circuit breakers B2 and B3	B2 and B3	B2 and B3
16	Short circuit between circuit breaker B3 and main bus	B3, CB14, and CB15	B3, CB12, and CB13

Figs. 2 and 3. The unidirectional circuit breaker trips only when the fault current flows in the direction of the arrow represented. In the following subsections, each fault is considered and the action of circuit breakers is explained.

A. Faults on the Transmission Network

In both PFTA 1 and 2, a fault in between the front-end active rectifier and circuit breakers (CB1_P, CB1_N) requires turning off the front-end active rectifier and tripping the circuit breakers CB2_P and CB2_N. By removing the gate pulses, the front-end active rectifier is disconnected. The circuit breakers CB2_P and CB2_N are tripped for two reasons, one is to protect the cable from short-circuit currents of the input dc link capacitors of dc–ac converters and the other is to prevent short circuit of generator interconnected from the other channel (connected via tiebreaker 1) since the generator of the unhealthy channel is disconnected. The circuit breakers CB1_P and CB1_N will not respond as the current flowing through them is opposite in direction. The circuit breakers CB1_P and CB1_N will trip if there is a fault in the cable between the circuit breakers {CB1_P, CB1_N} and {CB2_P, CB2_N} to prevent short-circuit currents from the front-end active rectifier output. These two faults will not affect the main bus but isolate the generator and the power to healthy motors is supplied using the generator of other channels. The isolation of the main bus is required if there is a fault at locations as mentioned in the previous section for both PFTA 1 and 2.

B. Faults on the Distribution Network

A fault in between circuit breakers {CB3_P, CB3_N} and {CB4_P, CB4_N} will trip the circuit breakers CB3_P, CB3_N, CB4_P, and CB4_N and isolate the motor M_L1. Similarly, the motors M_L2, M_R1, or M_R2 are isolated for the fault in between the circuit breakers (CB5_P, CB5_N, CB6_P, and CB6_N for distribution network 2, CB7_P, CB7_N, CB8_P, and CB8_N for distribution network 3, and
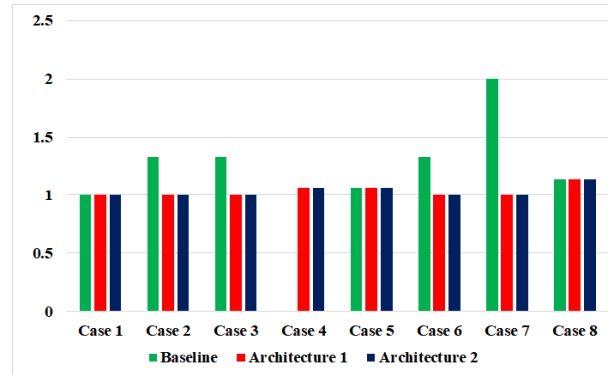

Fig. 4. Rating of motors for all architectures.

CB9_P, CB9_N, CB10_P, and CB10_N for distribution network 4) of corresponding distribution networks. The action of circuit breakers for other fault types of both PFTA 1 and 2 is listed in Table II.

V. SIZING OF COMPONENTS

This section discusses the sizing of various components that include generators, motors, circuit breakers, and cables for all architectures considering the different fault scenarios. Table III illustrates the sizing of motors for all the three architectures.

A. Motors and Generators

For different faults, the loading on each motor varies to provide the demanded power to run the electric aircraft. Based on this loading, the rating of the motors is decided. Table III shows the comparison of faults at different locations of the three architectures, which lead to oversizing of the components. The required rating of motor for cases mentioned in the table for all the three architectures is shown in Fig. 4.

It can be seen that the radial baseline architecture needs to be oversized to twice the rated value for case 7. This oversizing

TABLE III
SIZING OF MOTORS CONSIDERING DIFFERENT FAULTS

Cases	Fault type	Radial baseline architecture			PFTA -1			PFTA -2		
		Available power (MW)	Motors available (n)	Rating of motor (16 MW / n)	Available power (MW)	Motors availabl e (n)	Rating of motor (16 MW / n)	Available power (MW)	Motors available (n)	Rating of motor (16 MW / n)
1	Healthy system	16	16	1	16	16	1	16	16	1
2	Between CB1 and CB2	12	12	1.334	12	16	1	15	16	1
3	Main bus short	12	12	1.334	16	16	1	16	16	1
4	location LN (N = 1,2....)	-	-	-	16	15	1.0667	16	15	1.0667
5	Between CB3 and CB4	16	15	1.0667	16	15	1.0667	16	15	1.0667
6	One generator out of service	12	12	1.334	12	16	1	12	16	1
7	Two generators out of service	8	8	2	8	16	1	8	16	1
8	Two motors out of service	16	14	1.143	16	14	1.143	16	14	1.143
Maximum rating of the motor		Baseline		2 MW	PFTA 1		1.143 MW	PFTA 2		1.143 MW

of the motor requires the dc/ac converter, circuit breakers, and cables of the distribution networks to be able to withstand the currents flowing through them in case of this fault mentioned in case 7. However, PFTA 1 and 2 should be oversized by only 1.143 times the rated value, and thus, the cables, circuit breakers, and dc/ac converters need to be designed accordingly. Oversizing of PFTA 1 and 2 is much lower when compared with radial baseline architecture, which is described in Section V-B. Considering two generator outages as a worst case condition, the generators are oversized twice to meet the load requirements. The oversizing of the generators for PFTA 1 and 2 remains the same as in the case of radial baseline architecture.

B. Circuit Breakers and Cables

1) Distribution Network: The selection of circuit breakers and cables depends on the value of the current flowing them. The current flowing through circuit breakers in the distribution network is given in the following equation:

$$I_{dx} = \frac{P_{\text{motor}}}{V_{\text{inv}} * \eta_m * \eta_{\text{inv}}} \tag{1}$$

where I_{dx} represents the current through the xth distribution network. η_m and η_{inv} are the efficiencies of motor and dc–ac converter, respectively, P_{motor} represents the output power of motor, and V_{inv} is the voltage at the input of the inverter, which is 1000 V ($\pm$500 V). The efficiencies of the motor and dc–ac converter are assumed to be 95% and 98%, respectively, and the power rating of each motor is 2 MW (refer to case 7 in Table III) for radial baseline architecture and 1.143 MW (refer to case 8 in Table III) for PFTA 1 and 2. Using (1), the value of I_{d1} (current through distribution network 1) for distribution network 1 in radial baseline architecture and PFTA 1 or 2 is obtained as 2148.2 and 1227.8 A, respectively.

2) Transmission Network: In radial baseline architecture, the maximum current will flow through the transmission network in case 7 of Table III, and the expression is given by the following equations:

$$I_T = I_{d1} + I_{d2} + I_{d3} + I_{d4} + I_{\text{NP}} \tag{2}$$

$$I_{\text{NP}} = \frac{P_{\text{NP}}}{V_{\text{inv}}} \tag{3}$$

where I_{NP} represents the current through the NP load, and I_T represents the total current. I_{d1}, I_{d2}, I_{d3}, and I_{d4} represent the currents through distribution networks 1, 2, 3, and 4, respectively. A total of 1-MW power (P_{NP}) is required for NP loads and considering two generators outage (refer to case 7 in Table III), the NP loads are designed for 0.5 MW in each channel. During normal operation, power to NP loads will be shared equally (0.25 MW each) by all four generators. From (1) and (2), I_{NP} is 250 A and I_T is 9092.9 A. For PFTA 1 and 2, the current flowing through the transmission network will be maximum for case 7 in Table III (two generators outage) since only two generators need to supply the load. During this case, the motors available are 16, and hence, each motor consumes 1 MW of power. Each generator (only two generators available) needs to supply eight propulsion motors and NP loads. In this case, the current through the transmission network will be the sum of all eight distribution network currents and NP load currents and is shown in the following equations:

$$I_T = 8 * I_{d,\text{rated}} + 2 * I_{\text{NP}} \tag{4}$$

$$I_{d,\text{rated}} = \frac{P_{\text{rated}}}{V_{\text{inv}} * \eta_m * \eta_{\text{inv}}} \tag{5}$$

where $I_{d,\text{rated}}$ and $P_{d,\text{rated}}$ represent the rated current and power of distribution channel, respectively. A current of 1074.12 A ($I_{d,\text{rated}}$) will be flowing through each distribution network in this case and 9092.9 A will be flowing through the transmission network. From the above analysis, it is clear that the oversizing of transmission network circuit breakers and cables of all the three architectures is the same, but oversizing of PFTA 1 and 2 distribution network circuit breakers and cables can be reduced to 42.85% when compared with the radial baseline architecture. A total of 16 distribution networks consisting of 16 propulsion motors, 16 dc/ac converters, 64 circuit breakers, and 16 distribution cables need to be oversized, which in turn reduces the weight and space occupied.

Weight Estimate Analysis: This section presents the weight estimate analysis on the oversizing of various components required for all the three architectures and overall weight savings with the proposed architectures. While performing analysis, the power density for motors and generators used
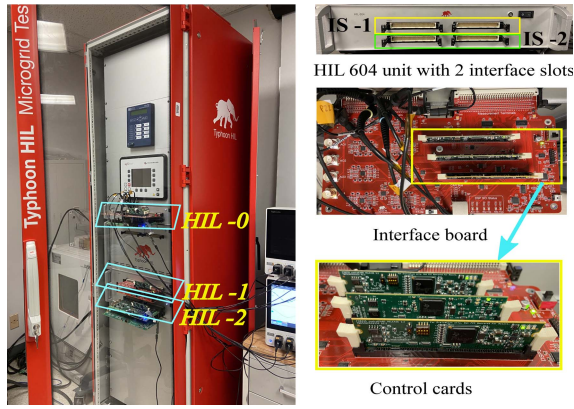
Fig. 5.   Typhoon HIL test setup.
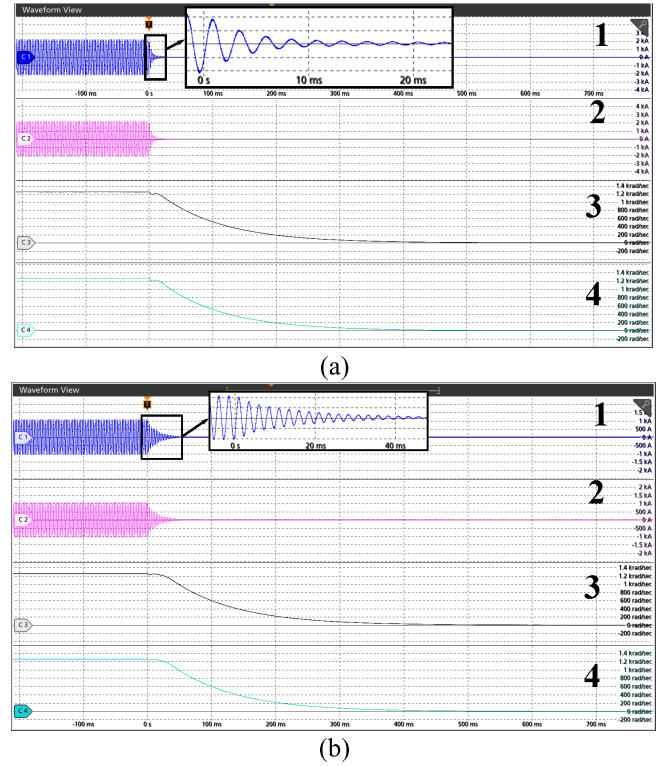

(a)

(b)

Fig. 6.   HIL results for open-circuit fault at main bus. (a) Rated load. (b) Half of the rated load. Time scale 100 ms/div. (1) Phase A current of motor M_L1 [(a) 1 kA/div and (b) 500 A/div]. (2) Phase A current of motor M_L2 [(a) 1 kA/div and (b) 500 A/div]. (3) Speed of the motor M_L1 (200 rad/sec/div). (4) Speed of the motor M_L2 (200 rad/sec/div).

in the architectures is taken as 13 kW/kg, while that of power electronic converters (ac/dc converter, dc/ac converter, and dc/dc converter) is 19 kW/kg. For cables, the specific ampacity is taken as 170 A/kg/m for a 0000-gauge copper for 1-kV system. The specific power for circuit protection is taken as 200 kW/kg. The weight of each component in each independent propulsion channel is calculated using the specific power values reported in [27]. From Table IV, it can be seen that the overall weight of the PFTA 1 and PFTA 2 is less when compared with the baseline architecture. It can also be seen that the overall weight savings with PFTA 1 and PFTA 2 are 841 and 759 kg, respectively, with respect to the existing baseline architecture.

VI. Results and Discussion

The proposed architectures considering different fault locations are validated using the CHIL results. As shown in Fig. 5, there are three HIL 604 devices in the testbed that are connected in parallel using the paralleling cables, each of which has two interface slots where typhoon HIL interface boards are being connected. In each of the typhoon HIL interface boards, there are three slots into which the control cards can be inserted. In this article, HIL 604 devices were used for modeling the system and TMDSCNCD28335 control cards are used for controlling the motors and circuit breakers in the system. The test conditions are listed in Table V, and the results for each fault in all the architectures are considered at $t = 0$.

A. Radial Baseline Architecture

1) Open-Circuit Fault: An open-circuit fault (positive/negative of cable is open) is created on the main bus of Fig. 1 at time $t = 0$ s. The circuit breakers in the transmission networks (CB1, B1) and distribution networks (CB4, CB6, CB8, and CB10) are tripped to isolate the main bus. The results corresponding to the open-circuit fault at rated are shown in Fig. 6(a). Upon the initiation of open-circuit fault, the phase current of motors M_L1 and M_L2 is seen to reduce to zero. The speed of motors M_L1 and M_L2 also drops from 1256 rad/s (12 000 r/min) to zero rad/s, indicating no power transfer to motors M_L1 and M_L2. Furthermore, the

load on the motors is reduced, and then, the open-circuit fault is created on the main bus at time $t = 0$ s to observe the behavior of the architecture, and the corresponding results are shown in Fig. 6(b). From results, it can be seen that currents of motors M_L1 and M_L2 reduce to zero as the circuit breakers in transmission and distribution networks are tripped. The results corresponding to that of motors M_R1 and M_R2 are the same as that of motor M_L2 for both the cases corresponding to rated and half the rated load conditions and hence are omitted. From these two case, it is clear that all the motors are disconnected for a fault on the main bus, with the radial baseline architecture.

2) Short-Circuit Fault: Furthermore, a short-circuit fault is created on the main bus at time $t = 0$ s (refer to Fig. 1), and the results are shown for rated load in Fig. 7(a) and for half the rated load is shown in Fig. 7(b). At both the loads, the circuit breakers in the transmission network and distribution network are tripped to protect the cables from the short-circuit currents. From the results, it is clear that for a short-circuit fault on the main bus, the A-phase currents and speed of both motors M_L1 and M_L2 are reduced to zero. The behavior of motors M_R1 and M_R2 is the same as that of motor M_L2. From both the fault cases, it is clear that the current flowing through the motor as well as the speed is tending to zero and thus losing all the four healthy motors. For the double faults (short circuit or open circuit) at the main bus, the results are similar to that of single fault on the bus and hence not shown. Thus, the

TABLE IV

COMPARISON OF WEIGHT ESTIMATES OF INDIVIDUAL CHANNEL FOR ALL THREE ARCHITECTURES

Components		Specific power (kW/kg)	Number	Power (kW)	Baseline (kg)	Number	Power (kW)	PFTA 1 (kg)	Number	Power (kW)	PFTA 2 (kg)
Generator		13	1	10000	769.23	1	10000	769.23	1	10000	769.23
Motor		13	4	2000	615.38	4	1143	351.69	4	1143	351.692
DC-AC converter		19	4	2000	421.052	4	1143	240.63	4	1143	240.631
AC-DC converter		19	1	10000	526.315	1	10000	526.31	1	10000	526.315
DC-DC converter		19	1	2000	105.26	1	2000	105.263	1	2000	105.263
Circuit breaker	Transmission	200	2	10000	100	2	10000	100	2	10000	100
	Distribution	200	8	2000	80	8	1143	45.72	8	1143	45.72
	main bus	200	-	-	-	10	10000	500	9	10000	450
Cable weight											
		A/kg/m	current	Weight	current	Weight		Current	Weight		
Cable	Transmission	170	8000	705.88	8000	705.882		8000	705.882		
	Distribution	170	2000	705.88	1143	403.412		1143	403.411		
	main bus	170	8000	141.176	8000	211.765		8000	282.353		
	Total weight (kg)			4170.18		3959.91			3980.5		

TABLE V

PARAMETERS USED

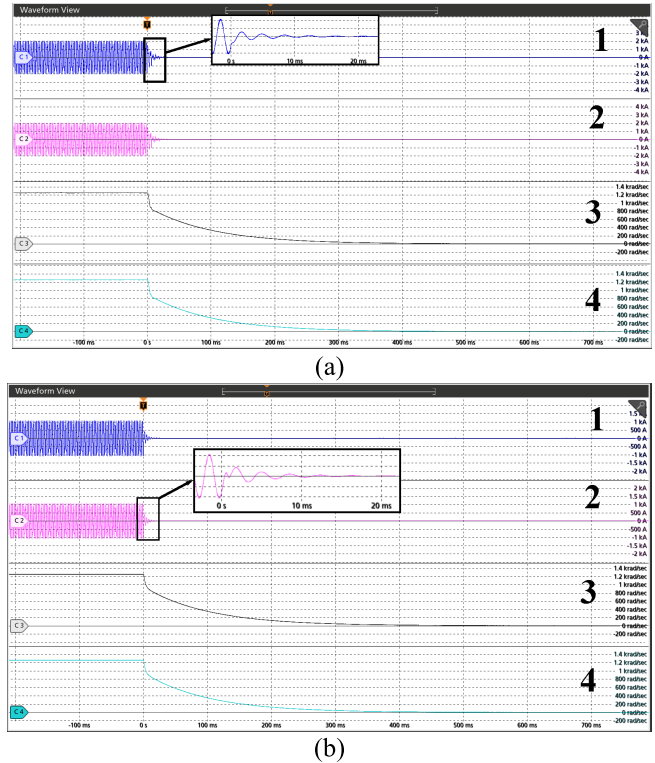| Parameters	Value
Bus voltage	± 500 V
Transmission network cable inductance (Lt)	100 μ H
Transmission network cable resistance (Rt)	0.02 Ω
Distribution network cable inductance (Ld)	50 μ H
Distribution network cable resistance (Rd)	0.01 Ω
Motor rating	1 MW
Non-propulsion loads	1 MW
Generator	5 MW
Motor speed (rad/sec)	1256
Frequency	400 Hz

(a)

(b)

Fig. 7. HIL results for short-circuit fault at main bus at (a) rated load and (b) half of the rated load. Time scale 100 ms/div. (1) Phase A current of motor M_L1 [(a) 1 kA/div and (b) 500 A/div]. (2) Phase A current of motor M_L2 [(a) 1 kA/div and (b) 500 A/div]. (3) Speed of the motor M_L1 (200 rad/sec/div). (4) Speed of the motor M_L2 (200 rad/sec/div).

operation using radial baseline architecture requires oversizing of all the components (motors, circuit breakers, converters, and cables) to meet the power demand lost as a result of isolation of healthy motors during open-/short-circuit faults.

B. PFTA 1

1) Open-Circuit Faults: The open-circuit fault is created on the bus at location L6 at time $t = 0$ s in PFTA 1, and the circuit breaker CB17 (refer Fig. 2) is tripped.

It is seen that the current and speed of motor M_L1 reduce to zero. However, the current and speed of motor M_L2 are not reduced to zero as the circuit breaker CB17 is tripped and is shown in Fig. 8(a). From this, it is clear that motor M_L1 alone is isolated from the architecture, but motor M_L2 remains in operation. The current and speed results of the motors M_R1 and M_R2 are identical to that of motor M_L2. For the open-circuit fault in the bus at location L8, the circuit breakers CB14 and CB15 are tripped. From the results shown
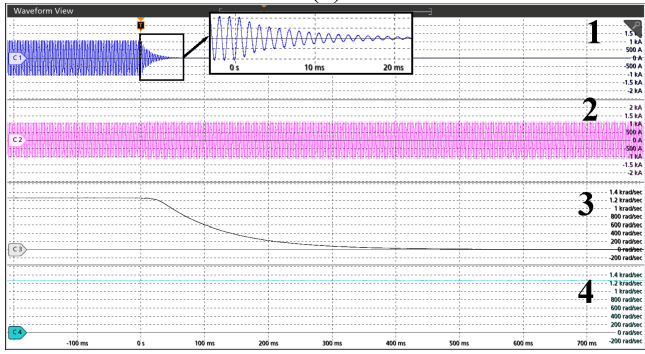
in Fig. 8(b), the phase A current and speed of motors M_L1 and M_L2 remain uninterrupted. Additionally, an open-circuit fault is created in PFTA 1 at half the rated load conditions, and the results shown in Fig. 8(c) indicate that only motor M_L1
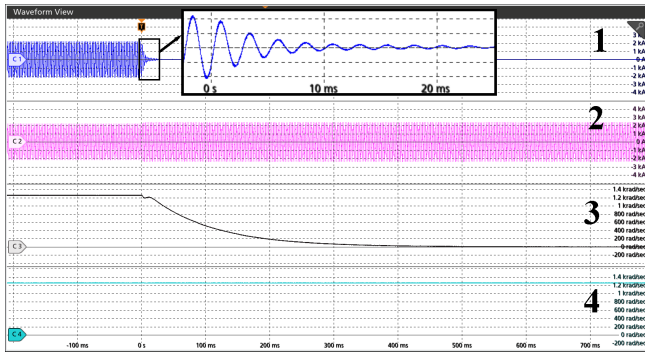
(a)
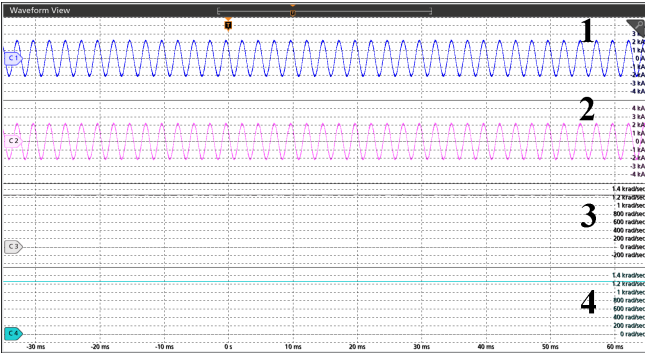
(b)

(c)

Fig. 8. HIL results for open-circuit fault. (a) Location L6 (at rated load). (b) Location L8 (at rated load). (c) Location L6 (at half of the rated load). Time scale 100 ms/div. (1) Phase A current of motor M_L1 [(a) and (b) 1 kA/div and (c) 500 A/div]. (2) Phase A current of motor M_L2 [(a) and (b) 1 kA/div and (c) 500 A/div]. (3) Speed of the motor M_L1 (200 rad/sec/div). (4) Speed of the motor M_L2 (200 rad/sec/div).

Fig. 9. HIL results for open-circuit fault at location L6 (rated load). Time scale 10 ms/div. (1) Phase A rms current of motor M_L1 (200 A/div). (2) Phase A rms current of motor M_L2 (200 A/div). (3) Phase A rms current of motor M_R1 (200 A/div). (4) Phase A rms current of motor M_R2 (200 A/div).

(a)

(b)

Fig. 10. HIL results for short-circuit fault at location L6 at (a) rated load and (b) half the rated load. Time scale 100 ms/div. (1) Phase A current of motor M_L1 [(a) 1 kA/div and (b) 500 A/div]. (2) Phase A current of motor M_L2 [(a) 1 kA/div and (b) 500 A/div]. (3) Speed of motor M_L1 (200 rad/sec/div). (4) Speed of motor M_L2 (200 rad/sec/div).

is isolated. From Fig. 9, it can be seen that the rms value of current through the phase A of motor during steady state is approximately 1.502 Ka, and after the fault, it is around 1.612 Ka, which is 1.073 times the nominal value.

2) Short-Circuit Fault: A single short-circuit fault is created at location L6 for both the rated load and half the rated load at time $t = 0$ s, the circuit breaker CB17 is tripped to protect the cable from short-circuit currents, and the results are shown in Fig. 10(a) and (b).

From the results, it can be seen that for both the rated and half rated loads, the current and speed of motor M_L1 tend to zero when the fault is created, and at the same time, the phase A current of motor M_L2 is increased indicating the increased power demand by the motor. In Fig. 11, the rms

value of phase A current before the fault is around 1.502 Ka and after the fault, it is 1.611 kA. From this, it can be inferred that, for a fault on the bus that isolates single motor, the current drawn by the remaining motors is approximately 1.073 times the current before fault, and hence, the motors has to be oversized by 7.3%. The results of motors M_R1 and M_R2 are the same as that of M_L2. Thus, comparing the PFTA 1 with the radial baseline architecture, PFTA 1 is capable of providing continuous power to the healthy motors by isolating the fault.
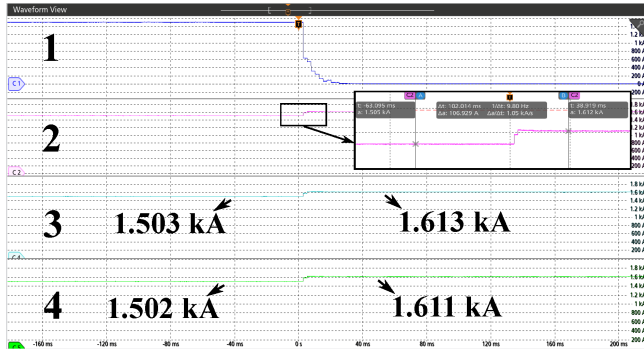
Fig. 11. HIL results for short-circuit fault at location L6 (rated load). Time scale 40 ms/div. (1) Phase A rms current of motor M_L1 (200 A/div). (2) Phase A rms current of motor M_L2 (200 A/div). (3) Phase A rms current of motor M_R1 (200 A/div). (4) Phase A rms current of motor M_R2 (200 A/div).
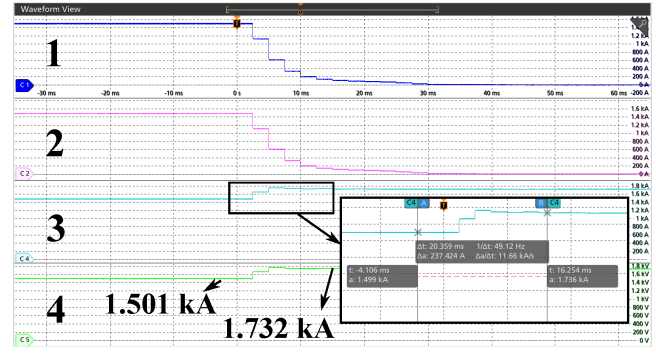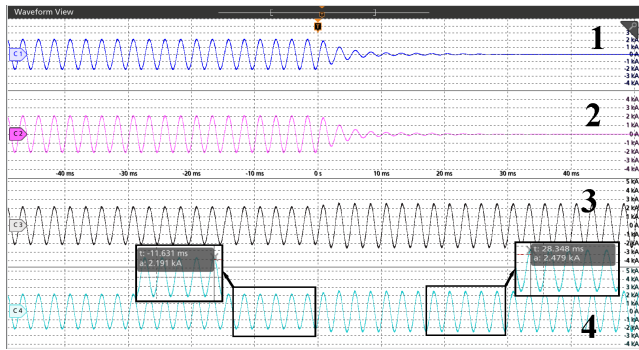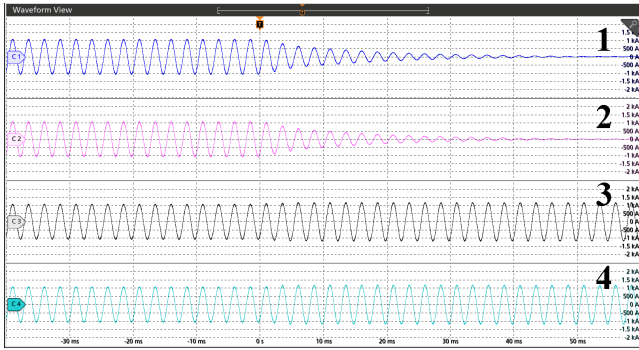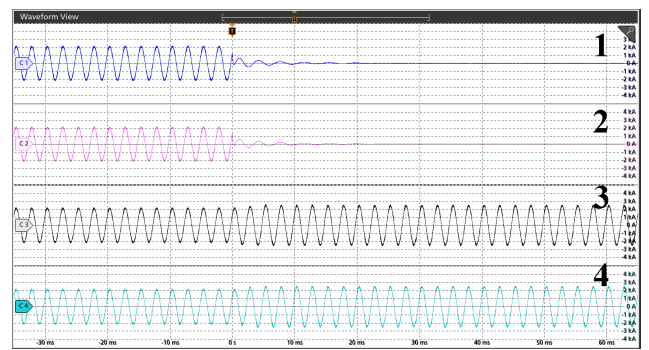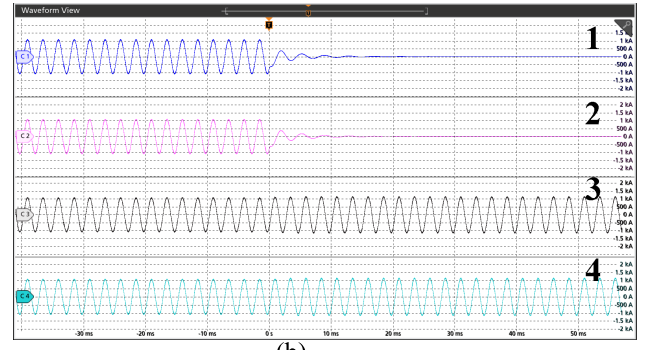

Fig. 13. HIL results for double open-circuit simultaneous fault at locations L5 and L6 (rated load). Time scale 10 ms/div. (1) Phase A rms current of motor M_L1 (200 A/div). (2) Phase A rms current of motor M_L2 (200 A/div). (3) Phase A rms current of motor M_R1 (200 A/div). (4) Phase A rms current of motor M_R2 (200 A/div).

Fig. 12. HIL results for double open-circuit simultaneous faults at locations L5 and L6. (a) Rated load. (b) Half the rated load. Time scale 10 ms/div. (1) Phase A current of motor M_L1 [(a) 1 kA/div and (b) 500 A/div]. (2) Phase A current of motor M_L2 [(a) 1 kA/div and (b) 500 A/div]. (3) Phase A current of motor M_R1 [(a) 1 kA/div and (b) 500 A/div]. (4) Phase A current of motor M_R2 [(a) 1 kA/div and (b) 500 A/div].

Fig. 14. HIL results for double short-circuit simultaneous faults at locations L5 and L6 at (a) rated load and (b) half the rated load. Time scale 10 ms/div. (1) Phase A current of motor M_L1 [(a) 1 kA/div and (b) 500 A/div]. (2) Phase A current of motor M_L2 [(a) 1 kA/div and (b) 500 A/div]. (3) Phase A current of motor M_R1 [(a) 1 kA/div and (b) 500 A/div]. (4) Phase A current of motor M_R2 [(a) 1 kA/div and (b) 500 A/div].

3) Double Open-Circuit Faults: The double open-circuit fault is created in PFTA 1 at simultaneous locations L5 and L6 at time $t = 0$ s for both rated and half rated loads, and the results are shown in Fig. 12(a) and (b), respectively. The currents through the motors M_L1 and M_L2 reduced to zero and the rms currents through motors M_R1 and M_R2 are increased from approximately 1.501 to 1.732 kA, as shown in Fig. 13. From the values, it can be inferred that the current through the healthy motors after fault is approximately 1.153 times the value of current before fault.

4) Double Short-Circuit Faults: A double short-circuit fault is created at locations L5 and L6 simultaneously at time $t = 0$ s for both rated load and half the rated loads, and corresponding typhoon HIL results are shown in Fig. 14(a) and (b), respectively. This results in isolation of motors M_L1 and M_L2 (circuit breakers CB15, CB16, and CB17 are tripped) and increase in the current of healthy motors M_L3 and M_L4 by 1.153 times the before fault value, as shown in Fig. 15, which is the same as the case with double open-circuit faults, since two of the motors are isolated.
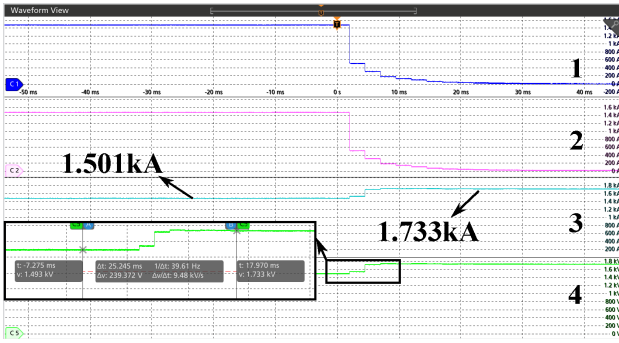
Fig. 15. HIL results for double short-circuit simultaneous fault at locations L5 and L6 (rated load). Time scale 10 ms/div. (1) Phase A rms current of motor M_L1 (200 A/div). (2) Phase A rms current of motor M_L2 (200 A/div). (3) Phase A rms current of motor M_R1 (200 A/div). (4) Phase A rms current of motor M_R2 (200 A/div).
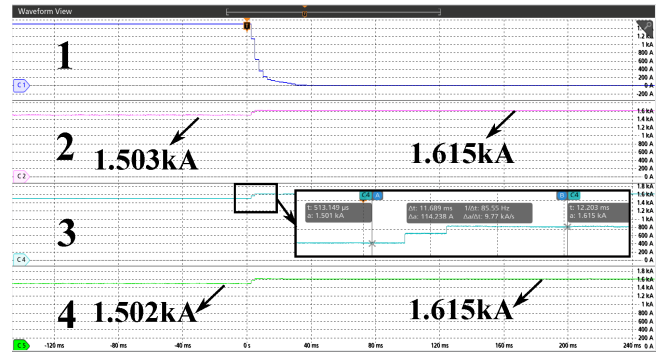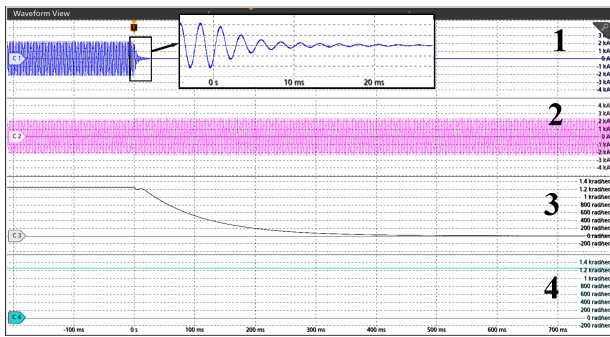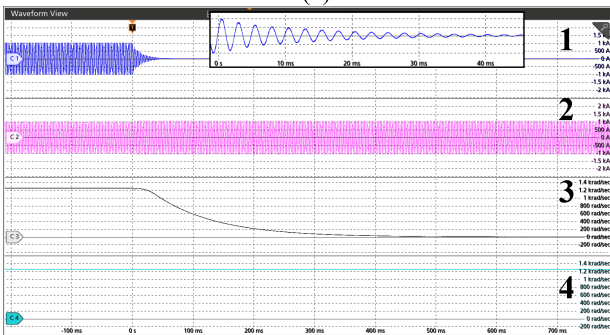

Fig. 17. HIL results for open-circuit fault at locations L4 (rated load). Time scale 40 ms/div. (1) Phase A rms current of motor M_L1 (200 A/div). (2) Phase A rms current of motor M_L2 (200 A/div). (3) Phase A rms current of motor M_R1 (200 A/div). (4) Phase A rms current of motor M_R2 (200 A/div).
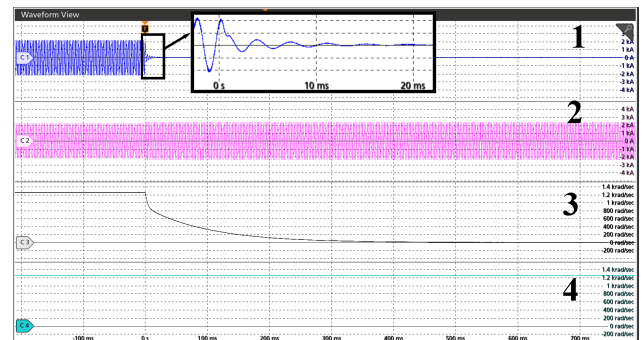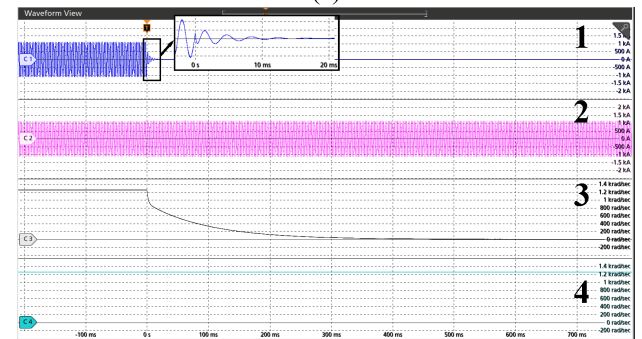

(a)

(b)

Fig. 16. HIL results for open-circuit fault at location L4 at (a) rated load and (b) half of the rated load. Time scale 100 ms/div. (1) Phase A current of motor M_L1 [(a) 1 kA/div and (b) 500 A/div]. (2) Phase A current of motor M_L2 [(a) 1 kA/div and (b) 500 A/div]. (3) Speed of the motor M_L1 (200 rad/sec/div). (4) Speed of the motor M_L2 (200 rad/sec/div).

(a)

(b)

Fig. 18. HIL results for short-circuit fault at location L4 at (a) rated load and (b) half of the rated load. Time scale 100 ms/div. (1) Phase A current of motor M_L1 [(a) 1 kA/div and (b) 500 A/div]. (2) Phase A current of motor M_L2 [(a) 1 kA/div and (b) 500 A/div]. (3) Speed of the motor M_L1 (200 rad/sec/div). (4) Speed of the motor M_L2 (200 rad/sec/div).

C. PFTA 2

1) Open-Circuit Fault: At location L4, an open-circuit fault is created at $t = 0$ s, and circuit breakers CB15 and CB14 are opened for the cases, where motors are operating at rated load and half rated load. The results corresponding to this fault are shown in Fig. 16(a) and (b). The current and speed of motor M_L1 are reducing to zero, which indicates that motor power is reducing to zero. The motor M_L2 continues to receive power for both the rated and half rated load conditions as the circuit breakers isolate the faulty section. For the open-circuit fault, the rms current through the motors has increased from

1.503 to 1.612 kA, which is 1.072 times the nominal value, as shown in Fig. 17.

2) Short-Circuit Fault: A short-circuit fault is created at location L4, and to isolate the fault, circuit breakers CB14 and CB15 are tripped, which results in disconnection of the motor shown in the A-phase current of motor M_L1 in Fig. 18(a) for rated load and in Fig. 18(b) for half the rated load.

It is clear from Fig. 19 that the healthy motors continue to operate with increased power of approximately 1.072 times the before fault value, and hence, this PFTA 2 allows the healthy
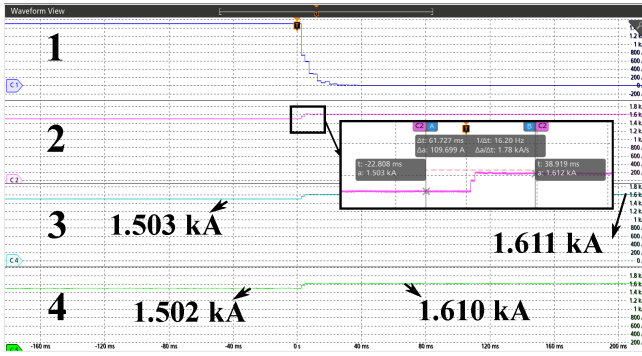
Fig. 19.   HIL results for short-circuit fault at locations L4 (rated load). Time scale 40 ms/div. (1) Phase A rms current of motor M_L1 (200 A/div). (2) Phase A rms current of motor M_L2 (200 A/div). (3) Phase A rms current of motor M_R1 (200 A/div). (4) Phase A rms current of motor M_R2 (200 A/div).
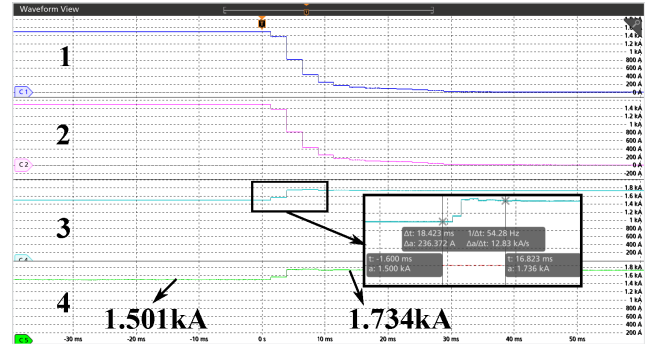

Fig. 21.   HIL results for double open-circuit simultaneous fault at locations L3 and L4 (rated load) Time scale 10 ms/div. (1) Phase A rms current of motor M_L1 (200 A/div). (2) Phase A rms current of motor M_L2 (200 A/div). (3) Phase A rms current of motor M_R1 (200 A/div). (4) Phase A rms current of motor M_R2 (200 A/div).
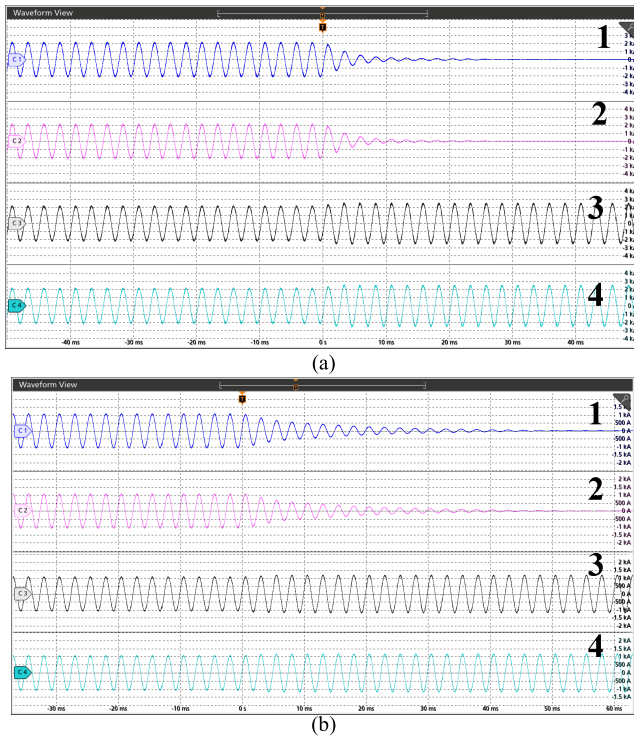

(a)

(b)

Fig. 20.   HIL results for double open-circuit simultaneous faults at locations L3 and L4 at (a) rated load and (b) half the rated load. Time scale 10 ms/div. (1) Phase A current of motor M_L1 [(a) 1 kA/div and (b) 500 A/div]. (2) Phase A current of motor M_L2 [(a) 1 kA/div and (b) 500 A/div]. (3) Phase A current of motor M_R1 [(a) 1 kA/div and (b) 500 A/div]. (4) Phase A current of motor M_R2 [(a) 1 kA/div and (b) 500 A/div].
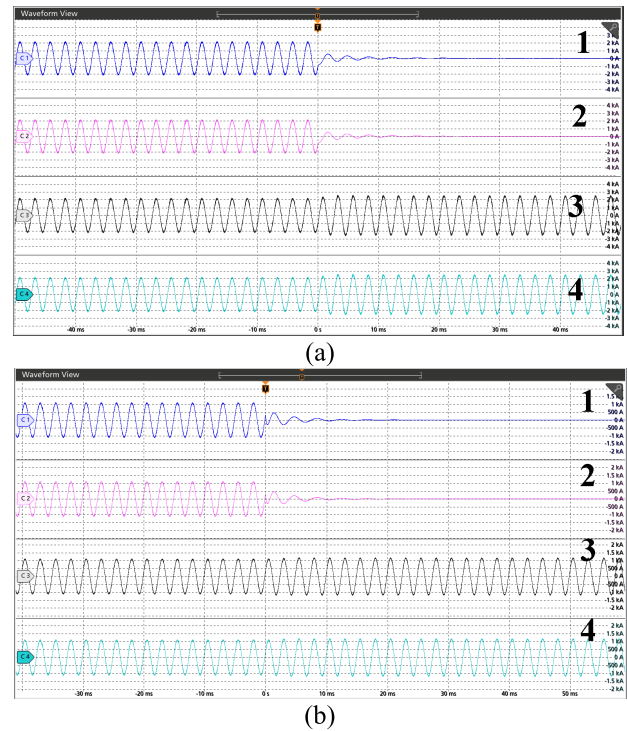

(a)

(b)

Fig. 22.   HIL results for double short-circuit simultaneous faults at locations L3 and L4 at (a) rated load and (b) half the rated load. Time scale 10 ms/div. (1) Phase A current of motor M_L1 [(a) 1 kA/div and (b) 500 A/div]. (2) Phase A current of motor M_L2 [(a) 1 kA/div and (b) 500 A/div]. (3) Phase A current of motor M_R1 [(a) 1 kA/div and (b) 500 A/div]. (4) Phase A current of motor M_R2 [(a) 1 kA/div and (b) 500 A/div].

motors to operate by isolating only the faulted section (L4 in this case).

3) Double Open-Circuit Faults: In PFTA 2, the double open-circuit faults are created simultaneously at locations L3 and L4, and then, the circuit breakers CB13, CB14, CB15, CBX_P, and CBX_N ($X = 4$, 6) are tripped to isolate the fault location and thus allowing motors M_R1 and M_R2 to operate as shown in the waveforms of Fig. 20(a) and (b) for both rated and half rated loads. The healthy motors draw a

power, which is 1.15 times greater than the value before fault as two of the motors are isolated, as shown in Fig. 21.

4) Double Short-Circuit Faults: The short-circuit faults are created simultaneously at locations L3 and L4 for rated load and half rated load conditions. The circuit breakers [CB13, CB14, CB15, CBX_P, and CBX_N ($X = 4$, 6)] are tripped to isolate the fault, and the results are shown in Fig. 22(a) and (b). From figures, it can be observed that the current through the motors M_L1 and M_L2 reduces to zero for both the load conditions. The motors M_R1 and M_R2 continue to receive the power as faulty location is
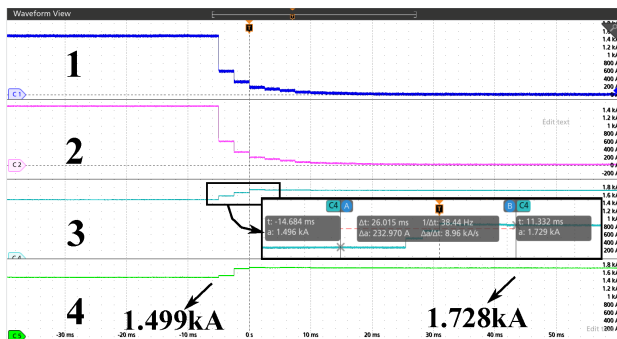
Fig. 23. HIL results for double short-circuit simultaneous fault at locations L3 and L4 (rated load). Time scale 10 ms/div. (1) Phase A rms current of motor M_L1 (200 A/div). (2) Phase A rms current of motor M_L2 (200 A/div). (3) Phase A rms current of motor M_R1 (200 A/div). (4) Phase A rms current of motor M_R2 (200 A/div).

isolated. The healthy motors draw nearly 15.5% more power than the power under normal operating conditions, as shown in Fig. 23, which implies that the motors have to be oversized by 15.5%. For both the short-circuit and open-circuit faults, the PFTA 2 results in enhanced fault-tolerant performance when compared to the existing radial baseline architecture by isolating the respective motors instead of isolating all the motors.

VII. Conclusion

This article proposes two architectures for enhanced bus protection in electric aircraft systems. The proposed architectures are designed using a loop-type structure in the main bus to isolate the faulty sections and allow the healthy propulsion motors to operate, thereby overcoming the limitations in the existing radial baseline architectures. From the results obtained, it is inferred that only 15.5% oversizing is required for the propulsion motors for both PFTA 1 and 2, whereas these motors need to be overrated by 100% with the baseline architecture. This implies that the proposed architectures reduce the oversizing of the propulsion motors by 42.25% when compared with the baseline architecture. This in turn reduces the current rating of distribution network circuit breakers also by 42.25%. From weight analysis, the estimated weight savings of the proposed architectures (PFTA 1 and 2) are approximately 841 and 759 kg, with respect to the baseline architecture. Thus, the proposed architectures provide enhanced fault protection, reduce oversizing, and increase efficiency, thus enabling further reduction in emissions.

References

[1] National Academies of Sciences, Engineering, and Medicine, *Commercial Aircraft Propulsion and Energy Systems Research: Reducing Global Carbon Emissions*. Washington, DC, USA: The National Academies Press, 2016, doi: 10.17226/23490.

[2] P. J. Ansell and K. S. Haran, "Electrified airplanes: A path to zero-emission air travel," *IEEE Electrific. Mag.*, vol. 8, no. 2, pp. 18–26, Jun. 2020, doi: 10.1109/MELE.2020.2985482.

[3] R. M. A. Valdés, S. Burmaoglu, V. Tucci, L. M. B. da Costa Campos, L. Mattera, and V. F. G. Comendador, "Flight path 2050 and ACARE goals for maintaining and extending industrial leadership in aviation: A map of the aviation technology space," *Sustainability*, vol. 11, no. 7, p. 2065, Apr. 2019, doi: 10.3390/su11072065.

[4] D. K. Hall, A. C. Huang, A. Uranga, E. M. Greitzer, M. Drela, and S. Sato, "Boundary layer ingestion propulsion benefit for transport aircraft," *J. Propuls. Power*, vol. 33, no. 5, pp. 1118–1129, Sep. 2017, doi: 10.2514/1.B36321.

[5] B. H. Nya, J. Brombach, and D. Schulz, "Benefits of higher voltage levels in aircraft electrical power systems," in *Proc. Electr. Syst. Aircr., Railway Ship Propuls.*, 2012, pp. 1–5, doi: 10.1109/ESARS.2012.6387381.

[6] J. Chen, C. Wang, and J. Chen, "Investigation on the selection of electric power system architecture for future more electric aircraft," *IEEE Trans. Transport. Electrific.*, vol. 4, no. 2, pp. 563–576, Jun. 2018, doi: 10.1109/TTE.2018.2792332.

[7] J. Brombach, A. Lucken, B. Nya, M. Johannsen, and D. Schulz, "Comparison of different electrical HVDC-architectures for aircraft application," in *Proc. Electr. Syst. Aircr., Railway Ship Propuls.*, 2012, pp. 1–6, doi: 10.1109/ESARS.2012.6387380.

[8] A. Barzkar and M. Ghassemi, "Electric power systems in more and all electric aircraft: A review," *IEEE Access*, vol. 8, pp. 169314–169332, 2020, doi: 10.1109/ACCESS.2020.3024168.

[9] T. C. Cano *et al.*, "Future of electrical aircraft energy power systems: An architecture review," *IEEE Trans. Transport. Electrific.*, vol. 7, no. 3, pp. 1915–1929, Sep. 2021, doi: 10.1109/TTE.2021.3052106.

[10] X. Lang, T. Yang, Z. Wang, C. Wang, S. Bozhko, and P. Wheeler, "Fault tolerant control of advanced power generation center for more-electric aircraft applications," *IEEE Trans. Transport. Electrific.*, early access, Jun. 29, 2021, doi: 10.1109/TTE.2021.3093506.

[11] J. Benzaquen, J. He, and B. Mirafzal, "Toward more electric powertrains in aircraft: Technical challenges and advancements," *CES Trans. Electr. Mach. Syst.*, vol. 5, no. 3, pp. 177–193, Sep. 2021, doi: 10.30941/CESTEMS.2021.00022.

[12] M.-C. Flynn, C. E. Jones, P. J. Norman, and G. M. Burt, "A fault management-oriented early-design framework for electrical propulsion aircraft," *IEEE Trans. Transport. Electrific.*, vol. 5, no. 2, pp. 465–478, Jun. 2019, doi: 10.1109/TTE.2019.2913274.

[13] S. Venuturumilli, F. Berg, L. Prisse, M. Zhang, and W. Yuan, "DC line to line short-circuit fault management in a turbo-electric aircraft propulsion system using superconducting devices," *IEEE Trans. Appl. Supercond.*, vol. 29, no. 5, pp. 1–6, Aug. 2019, doi: 10.1109/TASC.2019.2909206.

[14] J. Menu, M. Nicolai, and M. Zeller, "Designing fail-safe architectures for aircraft electrical power systems," in *Proc. AIAA/IEEE Electr. Aircr. Technol. Symp. (EATS)*, Jul. 2018, pp. 1–14.

[15] C. L. Bowman, T. V. Marien, and J. L. Felder, "Turbo- and hybrid-electrified aircraft propulsion for commercial transport," in *Proc. AIAA/IEEE Electr. Aircr. Technol. Symp.*, Jul. 2018, pp. 1–8.

[16] NASA. *Electrified Aircraft Propulsion (EAP) for Larger Aircraft*. Accessed: Dec. 4, 2021. [Online]. Available: https://www1.grc.nasa.gov/aeronautics/eap/airplane-concepts/hybrid-electric/

[17] NASA. *Electrified Aircraft Propulsion (EAP) for Larger Aircraft*. Accessed: Dec. 4, 2021. [Online]. Available: https://www1.grc.nasa.gov/aeronautics/eap/airplane-concepts/partially-turboelectric/

[18] NASA. *Electrified Aircraft Propulsion (EAP) for Larger Aircraft*. Accessed: Dec. 4, 2021. [Online]. Available: https://www1.grc.nasa.gov/aeronautics/eap/airplane-concepts/turboelectric/

[19] H. D. Kim, J. L. Felder, M. T. Tong, and M. Armstrong, "Revolutionary aeropropulsion concept for sustainable aviation: Turboelectric distributed propulsion," Tech. Rep. ISABE-2013-1719, Sep. 2013.

[20] M. J. Armstrong, C. A. H. Ross, M. J. Blackwelder, and K. Rajashekara, "Trade studies for NASA N3-X turboelectric distributed propulsion system electrical power system architecture," *SAE Int. J. Aerosp.*, vol. 5, no. 2, pp. 325–336, Oct. 2012, doi: 10.4271/2012-01-2163.

[21] M. J. Armstrong *et al.*, "Architecture, voltage, and components for a turboelectric distributed propulsion electric grid," Tech. Rep. NASA/CR-2015-218440, 2015.

[22] M. J. Armstrong, M. Blackwelder, and C. Ross, "Sensitivity of TeDP microgrid system weight and efficiency to operating voltage," in *Proc. 50th AIAA/ASME/SAE/ASEE Joint Propuls. Conf.*, 2014, p. 3492, doi: 10.2514/6.2014-3492.

[23] M. J. Armstrong, C. A. H. Ross, M. J. Blackwelder, and K. Rajashekara, "Propulsion system component considerations for NASA N3-X turbo-electric distributed propulsion system," *SAE Int. J. Aerosp.*, vol. 5, no. 2, pp. 344–353, Oct. 2012, doi: 10.4271/2012-01-2165.

[24] M. J. Armstrong and C. A. H. Ross, "Power and protection considerations for TeDP microgrid systems," *Aircr. Eng. Aerosp. Technol.*, vol. 86, no. 6, pp. 509–514, Sep. 2014, doi: 10.1108/AEAT-04-2014-0049.

[25] Y. Bai and A. Rajapakse, "Fault detection and localization in a ring bus DC microgrid using current derivatives," in *Proc. IEEE Can. Conf. Electr. Comput. Eng. (CCECE)*, Aug. 2020, pp. 1–6, doi: 10.1109/CCECE47787.2020.9255718.

[26] J.-D. Park, J. Candelaria, L. Ma, and K. Dunn, "DC ring-bus microgrid fault protection and identification of fault location," *IEEE Trans. Power Del.*, vol. 28, no. 4, pp. 2574–2584, Oct. 2013, doi: 10.1109/TPWRD.2013.2267750.

[27] Z. Zhang, Q. Chen, R. Xie, and Y. Zheng, "A protection system for improved ring-bus DC microgrids," *Energies*, vol. 12, no. 19, p. 3778, Oct. 2019, doi: 10.3390/en12193778.

[28] R. Jansen, C. Bowman, and A. Jankovsky, "Sizing power components of an electrically driven tail cone thruster and a range extender," in *Proc. 16th AIAA Aviation Technol., Integr., Operations Conf.*, Reston, Virginia, Jun. 2016, p. 3766.

Anil Kumar Reddy Siddavatam (Graduate Student member, IEEE) received the bachelor's degree in electrical and electronics engineering from Sree Vidyanikethan Engineering College, Tirupati, India, in 2017, and the master's degree in power electronics from the National Institute of Technology, Calicut, India, in 2020. He is currently pursuing the Ph.D. degree with the Department of Electrical and Computer Engineering, University of Houston, Houston, TX, USA.

He worked as a PGET (Design Engineer) with Research Center, Power Transmission & Distribution IC, L&T Constructions, Chennai, India, from August 2020 to July 2021. His research interests include switched mode power supplies and protection for aerospace applications.

Kaushik Rajashekara (Life Fellow, IEEE) received the Ph.D. degree in electrical engineering from the Indian Institute of Science, Bengaluru, India, in 1984.

In 1989, he joined the Delphi Division, General Motors Corporation, Indianapolis, IN, USA. In Delphi and General Motors, he held various lead technical and managerial positions, and the Chief Scientist for propulsion systems for electric, hybrid, and fuel cell vehicles. In 2006, he joined Rolls-Royce Corporation, Indianapolis, as a Chief Technologist for electric systems for electric and hybrid aircraft systems. In 2012, he joined as a Distinguished Professor of engineering with the University of Texas at Dallas, Richardson, TX, USA. Since 2016, he has been a Distinguished Professor of engineering in the University of Houston, Houston, TX. His research interests include power/energy conversion, transportation electrification, renewable energy, and microgrid systems.

Dr. Rajashekara is a member of the U.S. National Academy of Engineering. He has received a number of awards including IEEE Medal on Environment and Safety Technologies for his contributions to electrification of transportation and renewable energy.

Ravi Prakash Reddy received the B.Tech. degree in electrical engineering from the National Institute of Technology, Calicut, India, in 2015, and the M.Sc. degree in engineering and the Ph.D. degree from the Indian Institute of Science, Bengaluru, India, in 2020.

He is currently working as a Post-Doctoral Fellow at the Department of Electrical and Computer Engineering, University of Houston, Houston, TX, USA. His research interests include high-performance control and self-commissioning of induction motor drives and high-voltage gain dc–dc power electronic converters for electric vehicle applications.

Hao Huang (Life Fellow, IEEE) received the Ph.D. degree in electrical engineering from the University of Colorado at Boulder, Boulder, CO, USA, in 1987.

He was Technology Chief of GE Aviation—Electrical Power and has 35 years of experience in Aircraft Electrical Power Systems and Power Generation. He has been Retired since May of 2020. He was responsible for generating the technical directions, innovation strategies, and multigeneration product roadmaps for the GE aircraft electrical power division. Since July 2020, he has been a Distinguished Adjunct Professor with the University of Houston, Houston, TX, USA, and an Adjunct Professor with WEMPEC, University of Wisconsin–Madison, Madison, WI, USA. He has over 70 U.S. patents.

Dr. Huang is an NAE Member and SAE Fellow. He is the recipient of 2019 IEEE Transportation Technologies Award.

Harish S. Krishnamoorthy (Senior Member, IEEE) received the B.Tech. degree from the Department of Electrical and Electronics Engineering, National Institute of Technology (NIT), Tiruchirappalli, India, in 2008, and the Ph.D. degree from Texas A&M University, College Station, TX, USA, in 2015.

From 2008 to 2010, he worked in GE Energy, Noida, India. Since August 2017, he joined the University of Houston (UH), Houston, TX, as an Assistant Professor. He has about 80 journal/conference papers. He was also named an "OTC Emerging Leader" by the Offshore Technology Conference, 2022. His research interests are high-density power conversion for grid interface, statistical and machine learning-based methods in power electronics, 4G/5G envelope tracking, and so on.

He received the UH Cullen College of Engineering's Teaching Excellence Award in 2021 and Research Excellence Award in 2022. He is also an Associate Editor of the IEEE TRANSACTIONS ON POWER ELECTRONICS.
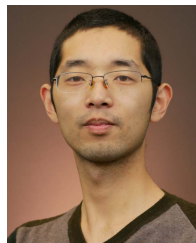
Zhou Dong (Member, IEEE) received the B.S. and M.S. degrees in electrical engineering from the Nanjing University of Aeronautics and Astronautics, Nanjing, China, in 2014 and 2017, respectively, and the Ph.D. degree from the University of Tennessee, Knoxville, TN, USA, in 2022.

He is currently a Power Electronics Scientist at ABB U.S. Corporate Research Center, Raleigh, NC, USA. His research interests include wide bandgap semiconductor device applications, electrical power system protection, and design automation in power electronics.

Fei (Fred) Wang (Fellow, IEEE) received the B.S. degree in electrical engineering from Xi'an Jiaotong University, Xi'an, China, in 1982, and the M.S. and Ph.D. degrees in electrical engineering from the University of Southern California, Los Angeles, CA, USA, in 1985 and 1990, respectively.

He was a Research Scientist with the Electric Power Laboratory, University of Southern California, from 1990 to 1992. From 1992 to 2000, he worked with General Electric Industrial Systems and GE Research in various capacities. In 2001, he joined the Center for Power Electronics Systems, Virginia Tech, Blacksburg, VA, USA, as a Research Associate Professor, and also served as the CPES Technical Director from 2003 to 2009. Since 2009, he has been with the University of Tennessee, Knoxville, TN, USA, and Oak Ridge National Laboratory, Knoxville, TN, as Condra Chair Professor of Excellence in Power Electronics. His research interests include wide bandgap power electronics and power electronics applications for transportation and electric grid.

Dr. Wang is a Fellow of the U.S. National Academy of Inventors.